

Surface resonances versus surface states on Fe(110)

J. Braun,¹ C. Math,^{1,2} A. Postnikov,³ and M. Donath¹

¹*Physikalisches Institut, Westfälische Wilhelms-Universität Münster, Wilhelm-Klemm-Strasse 10, D-48149 Münster, Germany*

²*Max-Planck-Institut für Plasmaphysik, EURATOM Association, Surface Physics Division, D-85740 Garching bei München, Germany*

³*Fachbereich Physik, Universität Duisburg, D-47048 Duisburg, Germany*

(Received 13 August 2001; revised manuscript received 23 January 2002; published 23 April 2002)

The spin-dependent surface electronic structure of ferromagnetic Fe(110) is investigated experimentally and theoretically. Spin-resolved, inverse-photoemission results show a complex multipeak structure close to the Fermi level. Part of it is surface derived with an unexpected spin dependence and light-polarization dependence. The puzzling experimental findings are interpreted on the basis of a comprehensive theoretical analysis. Electronic slab calculations find surface-related features, caused by the crystal–vacuum interface, only well below the Fermi level. Calculations of the (inverse) photoemission intensities within the relativistic one-step model based on a bulk band structure, but with a realistic surface barrier, reveal an additional surface resonance around the Fermi level. Its nearly vanishing exchange splitting at $\bar{\Gamma}$ and abnormal energy dispersion behavior as a function of the wave vector parallel to the surface are in accordance with the experimental findings.

DOI: 10.1103/PhysRevB.65.184412

PACS number(s): 75.70.Rf, 73.20.–r, 75.50.Bb, 79.60.–i

I. INTRODUCTION

The discovery of new and fascinating properties that appear in magnetic systems of reduced dimension, triggered experimental as well as theoretical investigations to describe the observed phenomena on the basis of the spin-dependent electronic structure.¹ With decreasing size of the magnetic structures, surface and interface effects become more and more important and so does the surface and interface electronic structure. Photoemission (PE) and inverse-photoemission (IPE) probe the states in the vicinity of the Fermi level E_F , which are responsible for a variety of material properties, in particular, for the magnetic moments of the 3d ferromagnets Fe, Co, and Ni. While many investigations are devoted to more and more complicated systems during recent years, the present study deals with the relatively simple Fe(110) surface whose electronic structure is controversially discussed up till now. Inspecting the literature an extensive IPE database is available for simple metals, collected by several experimental and theoretical groups,² but only few studies deal with ferromagnets. Here we focus on the unoccupied states, using the experimental technique of spin-resolved IPE that has been developed into a powerful tool over the last almost 20 years.^{3,4}

On ferromagnets, crystal-induced surface states may directly contribute to the magnetic properties of the surface, provided they are exchange split with a nonequal occupation of the majority and minority components.^{5,6} In contrast, exchange-split surface states with both majority and minority components completely filled or empty serve as sensors of the surface magnetic properties but do not influence the net spin density responsible for the magnetic moment.^{7–10} Since Ni(111) and Co(0001) with their hexagonal surface geometry exhibit surface-derived states close to the Fermi level,^{5,11–15} a similar behavior is expected for the Fe(110) surface with its twofold but almost hexagonal symmetry. However, the experimental results reported for Fe(110) so far are not conclusive with respect to crystal-induced surface states. Apart

from very few exceptions, the measurements are successfully described on the basis of bulk-band transitions alone.^{16–20} One spin-integrated PE study, however, reports on a surface state at 0.15 eV below E_F at $\bar{\Gamma}$.²¹ In another PE investigation with spin resolution, a minority surface feature was observed at 0.5 eV below E_F at $0.5\bar{\Gamma}\bar{H}$,²² which was predicted by a tight-binding calculation.²³ In the calculations, the surface state starts from 0.4 eV above the Fermi level at $\bar{\Gamma}$ and disperses to lower energies along the $\bar{\Gamma}\bar{H}$ direction. Although the corresponding majority partner was predicted as well, it was not observed experimentally. Calculations within the one-step model of PE support the existence of a minority surface structure, whose appearance depends critically on the particular shape of the chosen surface potential.²⁴ Very recently, spin-resolved PE finds surface-sensitive features below E_F , which are interpreted as being 3d derived.²⁵ In spin-averaged^{26,27} and spin-resolved IPE measurements²⁸ no evidence of a surface-state emission close to E_F was found.

The identification of surface states close to E_F at ferromagnetic surfaces is more complex than at the simple metals owing to the 3d bands.²⁹ The unclear situation described above motivated us to start a detailed and comprehensive investigation of the surface electronic structure of Fe(110). To be able to distinguish unambiguously between image-potential-induced surface states and crystal-induced surface states and resonances, we decided for a combined theoretical analysis, which consists of both electronic slab and one-step photoemission calculations. The first method allows to identify surface states derived from bulk bands and caused by the crystal/vacuum cutoff. To deduce surface resonances, a sophisticated analysis with carefully defined criteria is needed. Such an analysis must be able to distinguish undoubtedly between surface states and resonances. Even with a successful identification, the $E(\mathbf{k}_{\parallel})$ dispersion that is sensitive to the shape of the surface barrier is not expected to be reproduced correctly. The calculated (I)PE spectra, on the other hand, use a realistic surface barrier and, in addition, give the spectral densities because they include also the matrix elements

of the related optical transitions. Thus, we are able to describe the energetics of image-potential states as well as crystal-induced surface resonances and surface states. A final comparison between both calculational schemes, in addition with a careful cross-check on the experimental data gives us the possibility to extract all resonancelike surface features that may exist on this metal surface. The paper is organized as follows. Section II describes the experimental details of our investigation. In Sec. III, the theoretical and computational methods are discussed, which are used in Sec. IV, where we present our experimental and theoretical results. A summary is given in Sec. V.

II. EXPERIMENTAL DETAILS

The Fe(110) surface was prepared as a 20-ML-thick bcc Fe film grown on a W(110) substrate. The Fe films were evaporated at a growth rate of 1 ML/min from a rod that was carefully cleaned by degassing at elevated temperatures. The cleaning process was continued over the whole experimental period to ensure also the removal of those bulk impurities that may have accumulated with time along the rod by diffusion. After the described degassing procedure the pressure during film preparation stayed below 1×10^{-10} mbar. Only these careful preparation conditions ensured the appearance of the electronic surface states that are described below. The (110) surface of bcc Fe, undistorted by the lattice misfit of the substrate, is observed for films thicker than 9 ML with low-energy electron diffraction (LEED) in accordance with earlier work.³⁰ IPE spectra show that the electronic bulk states are fully developed in films with a thickness of more than 15 ML. The substrate was held at room temperature during the deposition of the first 8 ML and then slowly raised to 550 K. At this temperature the deposited film was annealed for another 15 min to improve the surface structure.

The upper thickness limit of the films investigated is set by the thickness-dependent reorientation transition of the magnetic easy axis. For film thicknesses of more than 25 ML, the easy axis switches in the film plane from the $[1\bar{1}0]$ to the $[001]$ direction due to the decreasing influence of the surface anisotropy with film thickness.^{31,32} This reorientation transition can also be induced by adsorbates such as CO or O₂ at thicknesses lower than 25 ML.³¹ The interpretation of spin-resolved IPE spectra hinges on a defined angle between the spin polarization of the impinging electrons and the sample magnetization. In the experiment, the spin polarization of the electrons is a fixed parameter and is chosen to point into the $[1\bar{1}0]$ direction of the Fe films, which is also fixed in space. To guarantee under these experimental conditions a spin polarization parallel to the remanent sample magnetization, the thickness of the investigated films had to be chosen ≤ 20 ML. The magnetic state of the sample was investigated by spin-polarized secondary electron emission (SPSEE) using a focused electron beam for excitation and a spin-polarization detector (spin-polarized LEED detector) for analyzing the spin polarization of the emitted low-energy secondary electrons. The spin polarization of the secondary electrons is a measure of the sample magnetization.^{33–36} The remanent magnetization was found in a single-domain state

along the $[1\bar{1}0]$ direction with no indication for magnetic domain formation.

Spin-resolved IPE provides experimental access to the \mathbf{k} resolved, unoccupied, spin-dependent electronic structure. Spin-polarized electrons emitted from a GaAs photocathode impinge onto the sample with a defined angle. The divergence of the electron beam is estimated to be between 2° and 5°, depending on the actual parameters of the electron optics. The noncomplete spin polarization of about 30% is taken care of by normalization of the IPE spectra to hypothetical 100% spin polarization. The IPE-relevant decay channel for the incoming electrons are radiative transitions into lower-lying unoccupied states. The emitted photons are detected by energy-selective Geiger-Müller counters working as bandpass detectors. The bandpass is determined by the photoionization threshold of the iodine used as counting gas and the temperature-dependent transmission cutoff of the SrF₂ windows. The mean detection energies are 9.4 and 9.3 eV, depending on the temperature of the SrF₂ window, which is used as a parameter to influence the energy resolution.^{37,38} The overall energy resolution [FWHM (full width at half maximum)] combining the electron energy distribution and the detector bandpass width amounts to about 0.4 and 0.3 eV, respectively. Details about the spin-resolved IPE experiment are described elsewhere.^{3,39}

III. THEORETICAL DETAILS

A. Electronic structure

In our electronic structure analysis we use a slab geometry and the full-potential linearized augmented plane-wave method (see, e.g., Ref. 40), albeit implemented in the WIEN97 package.⁴¹ Differently from Wu and Freeman, we have included more atomic layers in the slab calculation. This, for example, allows the relaxation of the upper layer. We also used a generalized gradient approximation after Perdew-Burke-Ernzerhof⁴² for the exchange-correlation potential. To our opinion, a *muffin-tin* sphere size of 2.0 a.u. was used there. The surface layer relaxation in the five Fe layers is necessary to achieve bulk electronic properties (spin-resolved partial charges inside the spheres, density of states) in the central layer with an acceptable convergency. We tried 9-layer and 10-layer slab calculations; the results of the latter seem to be more smooth with regard to layer-dependent properties and therefore will be discussed below. The 10-layer slab supercell was constructed with the experimental value for the unit cell of iron $a = 2.87$ Å and has a z dimension of 26.70 Å, that roughly corresponds to three missing layers separating two slab surfaces. The top layer relaxation was allowed in normal direction, which in consequence resulted in an interlayer distance reduced by 12%. The spacing between deeper layers was kept fixed to that in the bulk. Based on the estimated force field in deeper layers, the second layer from the surface tends to relax slightly outwards, but we didn't perform the full relaxation throughout the slab. The cutoff parameters for the plane-wave basis selection $R_{MT}K_{max} = 8.5$ and for the charge-density Fourier expansion $G_{max} = 12.0$ would be probably not yet sufficient for

a more precise total-energy-based structure optimization. However, the band structure details, our primary concern are essentially converged with these cutoffs.

B. Photoemission

In order to calculate relativistic photoemission intensities, we start by solving the Dirac equation

$$\{c\hat{\alpha}\mathbf{p} + \beta c^2 + V(r) + \beta\hat{\sigma}\mathbf{B}(r) - E\}\Psi(\mathbf{r}) = 0. \quad (1)$$

In this expression $V(r)$ denotes the effective potential and $\mathbf{B}(r)$ the effective magnetic field. β is a 4×4 matrix, that fulfills $\beta^2 = 1$ and $\hat{\alpha}$ is a 4×4 Dirac matrix, which is defined by the 2×2 Pauli matrices σ_k , [$\alpha_k = \sigma_x \otimes \sigma_k$, ($k = x, y, z$)]. The Dirac equation itself can be obtained from the relativistic generalization of density-functional theory introduced by Rajagopal and Callaway⁴³ and Ramana and Rajagopal.⁴⁴ It can be solved using the phase-functional ansatz of Calogero⁴⁵ generalized to the relativistic case.⁴⁶⁻⁴⁹ From this solution it is easy to define the atomic scattering matrix Γ for a single ion-core potential together with the wave functions for the initial and for the final state. The atomic scattering matrix Γ together with the crystal geometry determines the scattering matrix M for a single layer. By means of layer-doubling techniques the so-called bulk-reflection matrix can be calculated, which gives the scattering properties of a semi-infinite stack of layers. Finally, applying the SPLEED theory⁵⁰⁻⁵⁸ we are able to derive the final state and the initial state for the semi-infinite crystal. According to Pendry⁵⁹ we have four different contributions to the relativistic photocurrent, which will be introduced in the following. The atomic contribution is built up by a product between the matrix \mathcal{Z}^1 and the multiple-scattering coefficients $A_{jn\kappa\mu}$ of the final state. Herein n denote the n th cell of the j th layer and κ, μ are the conventional relativistic indices. It follows:

$$I^a(\epsilon_f, \mathbf{k}_{\parallel}) \propto \text{Im} \sum_{jn} \sum_{\kappa\mu\kappa'\mu'} A_{jn\kappa\mu} \mathcal{Z}_{jn\kappa\mu\kappa'\mu'}^1 A_{jn\kappa'\mu'}^* \quad (2)$$

For an explicit calculation \mathcal{Z}^1 must be separated into angular matrix elements and radial double matrix elements. A detailed description of the matrix \mathcal{Z}^1 and of the multiple-scattering coefficients $A_{jn\kappa\mu}$ is given in Ref. 60. The intra(inter)layer contributions to the photocurrent describe the multiple-scattering corrections of the initial state between and within the layers of the single crystal. They can be written in a similar form

$$I^m(\epsilon_f, \mathbf{k}_{\parallel}) \propto \text{Im} \sum_{jn} \sum_{\kappa\mu\kappa'\mu'} A_{jn\kappa\mu} \mathcal{Z}_{jn\kappa\mu\kappa'\mu'}^2 C_{jn\kappa'\mu'}^{B,G} \quad (3)$$

Herein C^B and C^G denote the multiple-scattering coefficients of the initial state within a layer and between different layers. Analogously the matrix \mathcal{Z}^2 can be separated into angular and radial parts. The difference to the atomic contribution is that the radial part of the matrix \mathcal{Z}^2 consists of radial single matrix elements instead of radial double integrals. For a de-

tailed description of the matrix \mathcal{Z}^2 and of the multiple-scattering coefficients C^B and C^G the reader again is referred to Ref. 60.

Within the last contribution $I^s(\epsilon_f, \mathbf{k}_{\parallel})$ one takes care of the surface of the semi-infinite crystal. In particular, it follows for the surface part of the photocurrent:

$$I^s(\epsilon_f, \mathbf{k}_{\parallel}) \propto \text{Im} \int d\mathbf{r} \Psi_f^{*s}(\mathbf{r}) \Delta \Psi_i^s(\mathbf{r}), \quad (4)$$

with

$$\Psi_i^s(\mathbf{r}) = \int d\mathbf{r}' G_s^+(\mathbf{r}, \mathbf{r}') \Delta^* \Psi_f^s(\mathbf{r}'). \quad (5)$$

In the case of a z -dependent barrier potential $V_B = V_B(z)$, the initial- and final-state wave fields have to be calculated numerically in the surface region, as it has been shown by Grass *et al.*⁶¹ Both wave fields $\Psi_i^s(\mathbf{r})$ and $\Psi_f^s(\mathbf{r})$ can be decomposed into z dependent and corresponding parallel components

$$\Psi_i^s(\mathbf{r}) = \sum_{\mathbf{g}} \phi_{\mathbf{g}}(z) \exp[i\mathbf{k}_{i\mathbf{g}_{\parallel}}(\mathbf{r} - \mathbf{c})_{\parallel}], \quad (6)$$

$$\Psi_f^s(\mathbf{r}) = \sum_{\mathbf{g}} \chi_{\mathbf{g}}(z) \exp[i\mathbf{k}_{f\mathbf{g}_{\parallel}}(\mathbf{r} - \mathbf{c})_{\parallel}], \quad (7)$$

with the regular solutions of the Schrödinger equation $\phi_{\mathbf{g}}$ and $\chi_{\mathbf{g}}$ to the reciprocal lattice vector \mathbf{g} for $V_B(z)$ in the range $-\infty < z < c_z$. The value c_z defines the point, where the surface potential goes smoothly into the inner potential of the bulk crystal.

Final evaluation of the surface contribution gives

$$I^s(\epsilon_f, \mathbf{k}_{\parallel}) \propto \text{Im} \sum_{\mathbf{g}} e^{i\mathbf{q}_{\parallel} \cdot \mathbf{c}_{\parallel}} A_z \int_{-\infty}^{c_z} \psi_{\mathbf{g}} V_B' \chi_{\mathbf{g}} e^{iq_z z} dz, \quad (8)$$

where A_z is the z component of the amplitude \mathbf{A}_0 and \mathbf{q} is the wave vector of the photon field. For a step barrier $V_B(z) = V_{\text{or}} \Theta(z - c_{1z})$, where Θ is the unit step function, Pendry's result⁵⁹ will be reproduced. V_{or} denotes the constant inner potential of the bulk crystal.

At this stage some remarks concerning the computational details should be given. Lifetime effects in the final and initial states have been included in our analysis in a phenomenological way using a parametrized complex inner potential $V_o(E) = V_{\text{or}}(E) + iV_{\text{oi}}(E)$. Herein the real part serves as a reference energy inside the crystal with respect to the vacuum level. For the final and initial states constant imaginary parts $iV_{\text{oi}}(E_2) = 2.0$ eV and $iV_{\text{oi}}(E_1) = 0.01$ eV have been chosen. The bulk potential that we used in the photoemission calculations results from a tight-binding linear muffin-tin (TB-LMTO) method.^{62,63} A realistic description of the surface potential is given through a spin-dependent Rundgren-Malmström barrier,⁶⁴ which connects the asymptotic regime $z < z_A$ to the bulk muffin-tin zero V_{or} by a third-order polynomial in z , spanning the range $z_A < z < z_E$. The effective z -dependent surface barriers $V_B^{(1)}(z)$ for majority and minority spin are shown in Fig. 1. They are plotted

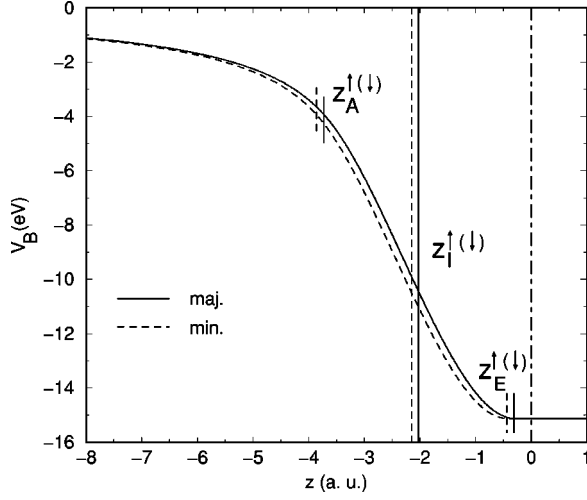


FIG. 1. Spin-dependent barrier potentials for Fe(110) from analysis of inverse-photoemission data. The majority and minority potential curves are shown as solid and dashed lines, respectively. The origin $z=0$, marked by the dot-dashed line represents the center of the first row of atoms. (For details see text.)

with respect to the vacuum level $E_{vac}=0.0$ eV utilizing the value of the work function $\phi=5.1$ eV.²⁸ The zero of the z scale lies in the uppermost layer of atoms. As mentioned above, $V_B^{\uparrow(l)}(z)$ are of the Rundgren-Malmström (RM) type.⁶⁴ For the real parts we have

$$V_B^{\uparrow(l)}(z) = \begin{cases} \frac{1}{4}(z - z_I^{\uparrow(l)})^{-1}, & z < z_A^{\uparrow(l)} < z_I^{\uparrow(l)} \\ s_0^{\uparrow(l)} + s_1^{\uparrow(l)}(z - z_A^{\uparrow(l)}) + s_2^{\uparrow(l)}(z - z_A^{\uparrow(l)})^2 + s_3^{\uparrow(l)}(z - z_A^{\uparrow(l)})^3, & z_A^{\uparrow(l)} < z < z_E^{\uparrow(l)} \\ V_{or}, & z > z_E^{\uparrow(l)}. \end{cases} \quad (9)$$

The imaginary part of the barrier potential has been set to zero avoiding the introduction of additional parameters. $z_I^{\uparrow(l)}$ denote the position of the classical spin-dependent image planes. The polynomial coefficients $s_0^{\uparrow(l)}, s_1^{\uparrow(l)}, s_2^{\uparrow(l)}, s_3^{\uparrow(l)}$ are fixed through the requirement of continuity and differentiability for $V_B^{\uparrow(l)}(z)$.

In order to exclude artificial parametrizations for the surface barrier, we followed the procedure described in detail in Ref. 15. The values of the three parameters z_I , z_A , and z_E that finally lead to a quantitative agreement between the measured and the calculated spectra are the following: $z_I^{\uparrow(l)} = -2.00$ (-2.15) a.u., $z_A^{\uparrow(l)} = -3.70$ (-3.85) a.u., and $z_E^{\uparrow(l)} = -0.30$ (-0.45) a.u.. The calculated intensity distributions have been multiplied with the Fermi function and convoluted with a Gaussian of FWHM=0.45 (0.35) eV to account for the finite resolution of the experiment.

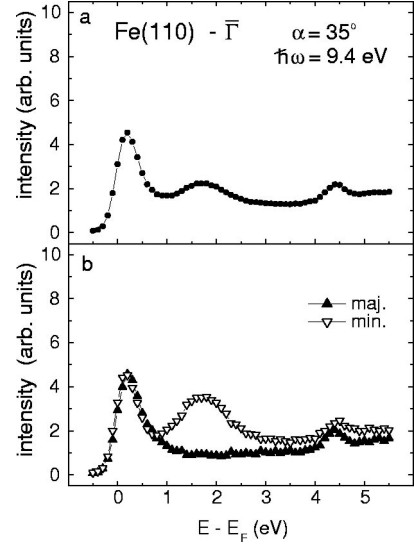


FIG. 2. Spin-integrated (a) and spin-resolved IPE spectra (b) obtained from a 20-ML-thick Fe(110) film on W(110). The photon takeoff angle was $\alpha=35^\circ$.

IV. RESULTS

A. Spectroscopic measurements

In Figs. 2 and 3, we present our spin-integrated and spin-resolved IPE data of the clean Fe(110) surface. The spectra were taken for normal electron incidence at two different photon takeoff angles $\alpha=35^\circ$ (Fig. 2) and $\alpha=70^\circ$ (Fig. 3). The spin-integrated spectra are shown in Figs. 2(a), 3(a) and the spin-resolved spectra in Figs. 2(b), 3(b). The spin-integrated data exhibit three distinct spectral features. The first one is located in energy just above the Fermi level, the second one at 1.8 eV, and the third one at about 4.5 eV above E_F . More detailed information is obtained from the spin-resolved data. The spin resolution allows us to identify five

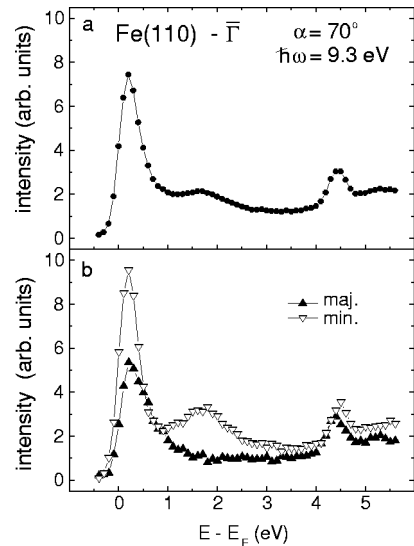


FIG. 3. Spin-integrated (a) and spin-resolved IPE spectra (b) obtained from a 20-ML-thick Fe(110) film on W(110). The photon takeoff angle was $\alpha=70^\circ$.

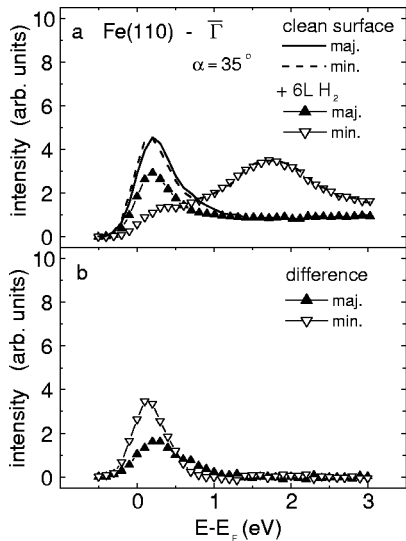


FIG. 4. Spin-resolved inverse-photoemission spectra for normal electron incidence on Fe(110). Spectra of the clean surface and of the surface exposed to 6 L of H_2 measured for $\alpha = 35^\circ$ (a). Corresponding difference spectra (b).

spectral features instead of three. The peak located just above the Fermi energy splits into a minority and a majority spectral feature. The second one is of pure minority character and is easily explained as minority d -band emission. The exchange-split peaks at about 4.5 eV above the Fermi level are the well-known spin partners of the $n = 1$ image-potential surface state.⁶⁵

The features close to the Fermi level appear at slightly different energies for spin-up and spin-down electrons. Their origin is investigated by exposing the surface to hydrogen. CO turned out to be not a suitable test adsorbate because, in contrast to experiments with the Ni(111) (Ref. 5) and Co(0001) (Ref. 15) surfaces, it quenches the bulk d -band emission as well. 6 L of H_2 do not affect the minority bulk emission but influence the features close to E_F in an elucidating way. The minority peak disappears completely while the majority peak is only partially quenched. The remaining majority feature is attributed to majority bulk d bands. The spin-resolved spectra of the clean surface (solid and dashed lines) together with the spectra of the surface exposed to hydrogen are shown in Figs. 4(a) and 5(a) for two different photon takeoff angles. The corresponding difference spectra, representing the surface-sensitive features, are displayed in Figs. 4(b) and Fig. 5(b). They reveal a minority structure and a smaller majority peak with a peculiar asymmetric line shape. The majority peak maximum appears at slightly higher energy than the maximum of the minority peak. This observation is in contrast to the expectation of a simple spin-split surface state with the minority-spin part higher in energy than the majority part.

B. Electronic slab calculations

The electronic structure of Fe(110) has been calculated on several occasions earlier. The energy bands of a thin film (represented by a 29-layer slab) have been calculated in 1976

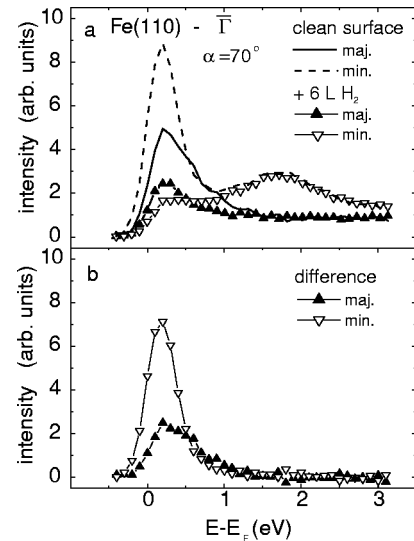


FIG. 5. Spin-resolved inverse-photoemission spectra for normal electron incidence on Fe(110). Spectra of the clean surface and of the surface exposed to 6 L of H_2 measured for $\alpha = 70^\circ$ (a). Corresponding difference spectra (b).

by Dempsey *et al.* who used a tight-binding scheme with matrix elements fitted to previous bulk calculations.²³ While fine details of the band structure may be slightly different in modern calculations, the thorough discussion about the symmetry composition of different bands in Ref. 23 are still useful. Freeman and Fu reviewed in Ref. 66 their calculations done with the full-potential linearized augmented plane-wave method on Fe(110), among other $3d$ metal surfaces. They used a 9-layer slab and found an enhancement of local magnetic moments towards the surface, from $2.22 \mu_B$ in the bulk to $2.65 \mu_B$ in the upper layer. Wu and Freeman⁶⁷ presented later a more detailed account of magnetism at the Fe(110) surface, based however on a calculation for a 7-layer slab. In Ref. 25 the authors interpreted their spin-resolved photoemission data in terms of a 23-layer slab calculation. To start with the discussion of surface specific features and their energy dispersion, we present in Fig. 6 the well-known band structure of bcc iron (thick dots) along with the additional bands (thin dots), which appear due to a folding into the two times smaller Brillouin zone (BZ) of the orthorhombic structure. The unit cell of the latter one is spanned by, e.g., $[\bar{1}10]$, $[001]$, and $[110]$. In consequence, it corresponds to pairwise repeated (110) planes. Therefore, the slab unit cell is constructed by these pairs. Taking into account more and more pairs of these planes, the Brillouin zone gets thinner and ultimately becomes two dimensional. The shape and the labeling of the bulk (bcc) and the surface (110) Brillouin zone is shown in the inset. Additionally to the bulk-related labeling of the high-symmetry lines in the bulk Brillouin zone, which is shown on the top of Fig. 6, the SBZ related labeling is visible at the bottom.

When analyzing the band dispersion in the supercell, we singled out projections of each eigenvector onto states with different angular momentum inside the muffin-tin radii, and correspondingly onto plane waves in the interstitial region. The contributions related to the Fe d states in the surface

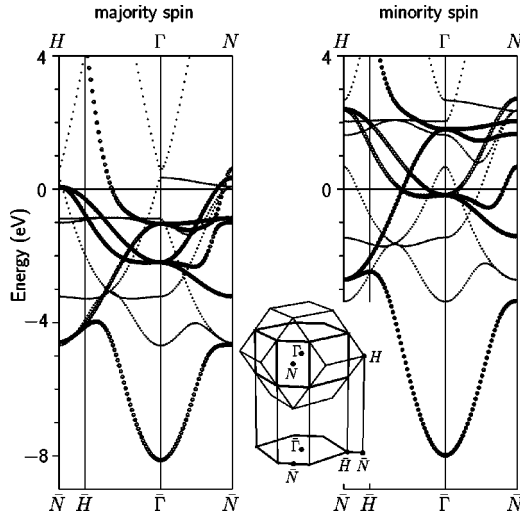


FIG. 6. Band structure of bcc iron, mapped onto the bcc bulk Brillouin zone (thick dots) and onto the orthorhombic Brillouin zone, corresponding to pairwise repeated (110) planes (thick and thin dots). Inset: Brillouin zone of the bcc lattice and of the bcc (110) surface.

layer are emphasized in Fig. 7 by the sizes of the dots. The most pronounced top-layer Fe *d* contributions appear in several bands in the vicinity of the Fermi level. These bands contain no contributions from deeper Fe layers, but instead a noticeable fraction coming from the states in the interstitial region. This fact is not really surprising, since the Fe muffin-tin spheres used in the calculation are relatively small. Therefore, one can identify the bands in question as essentially surface states. Specifically, in the minority-spin channel, we speak about two bands going upwards from the Fermi level along the Γ - \bar{N} direction, and another band that runs upwards from E_F along $\bar{\Gamma}$ - \bar{H} - \bar{N} . Similar features, shifted in energy, can be seen in the majority-spin channel (Fig. 7 left panel). Such surface states appear as well in the projected band structures calculated by the scattering-wave formalism *without* any additionally imposed surface barrier. This point will be discussed in more detail in the following section. One should notice, however, that all surface states that we found from the slab calculation are located in energy well below the Fermi level when concentrating on the vicinity of $\bar{\Gamma}$, i.e., restricting to normal electron incidence. As it has been discussed above, this result is in agreement with former investigations on Fe(110). On the other hand our inverse photoemission data, obtained in normal electron incidence, reveal strong intensity distributions for energies $E \geq E_F$, which should be related to surface features. The partial densities of states (DOS), resolved over Fe layers, are shown in Fig. 8. They have much in common with the results of Ref. 67. The DOS in the inner layers is well converged to that in the bulk, but the surface DOS is, however, markedly different: the shoulder at the Fermi level in the majority-spin DOS becomes less pronounced, and the dips separating a prominent upper peak of the bcc structure are smeared out. The magnetic moments increase towards the surface; their values related to muffin-tin spheres of Fe(1) to Fe(5) are 2.47, 2.29,

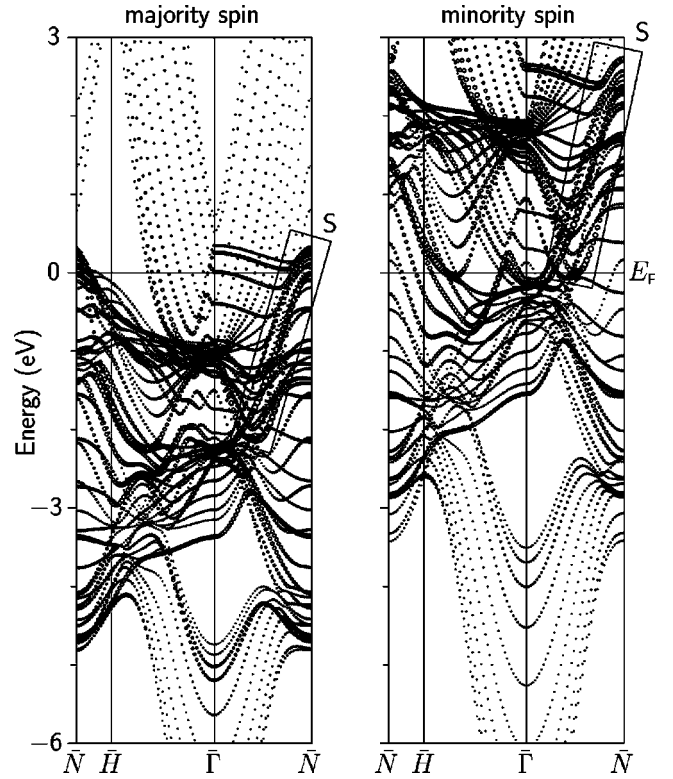


FIG. 7. Energy-band dispersion in the 10-layer supercell, with the upper layer relaxed by 12% inwards. Dot sizes indicate contributions from the surface Fe atoms.

2.32, 2.26, and $2.22 \mu_B$. These values agree well with the data of Freeman and Fu⁶⁶ for inner layers, but the magnitude of the magnetic moment on the surface is in our case somehow suppressed, probably as a consequence of inward relax-

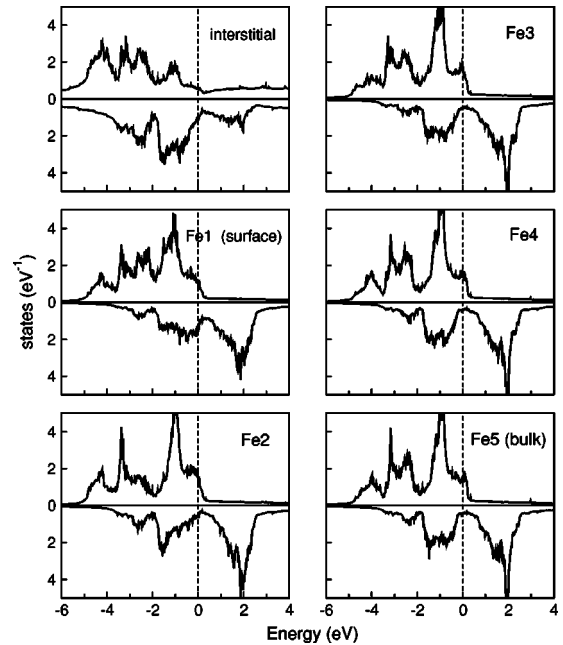


FIG. 8. Local densities of states in the supercell, resolved by (110) layers.

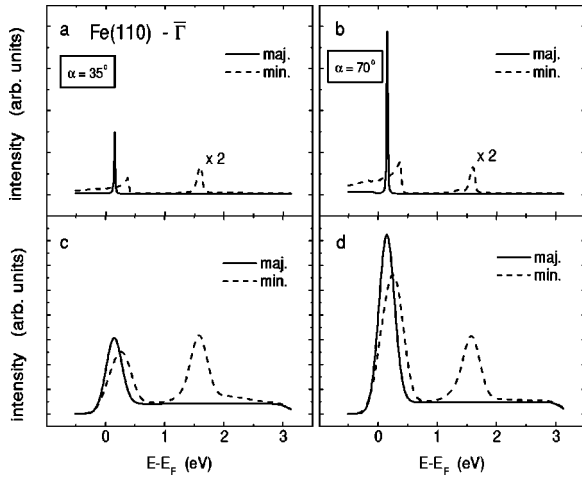


FIG. 9. Normal emission spectra calculated for light detection angles $\alpha=35^\circ$ (a) and $\alpha=70^\circ$ (b). (c) and (d) as (a) and (b) but multiplied with the Fermi function at room temperature and convoluted with Gaussians of FWHM=0.45 (0.35) eV.

ation we take into account. The spin density in the interstitial region (and outside the crystal) is slightly antiparallel, summing up to $-0.11 \mu_B$. A slight antiparallel magnetization in the vacuum region close to the surface has been already mentioned by Wu and Freeman.

C. One-step calculations

A detailed theoretical analysis within the one-step model of inverse photoemission gives us the following unexpected result. There is a surface structure just above the Fermi level with the majority part lying lower in energy than the minority ones. This is shown in Figs. 9(a) and 9(b) for both photon takeoff angles. The solid (dashed) lines represent the majority (minority) parts of the total intensity distribution. Because of the strong amount of surface emission the minority d -band transition has been increased by a factor of 2. At first one can observe that the majority part of the surface structure depends much more on the angle of light detection than the minority bulk peak does. The latter one is only slightly affected by a change of the detector angle. The majority feature exhibits a pronounced increase of spectral weight when increasing the z component of the vector potential A_z , i.e., switching from $\alpha=35^\circ$ to $\alpha=70^\circ$. The minority part of the unoccupied surface peak does not depend so strongly on A_z , indicating different symmetry properties of these two structures. A quantitative comparison with the experimental data requires a multiplication of the calculated raw spectra with the Fermi function. Also the convolution with a Gaussian is appropriate in order to simulate the finite experimental energy resolution. The final result is shown in Figs. 9(c) and 9(d). It is clearly observable from these figures that still some discrepancies with the experiment exist. The exchange splitting $\Delta_{ex}=0.25$ eV calculated for normal electron incidence is not in agreement with the slightly reversed spin splitting observed experimentally. Also, the relative intensities, which we obtained for the two spin channels do not reflect the experimental findings. For example, the intensity ratio be-

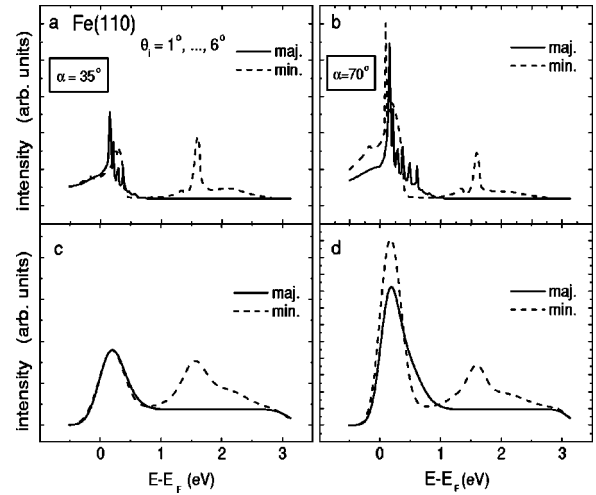


FIG. 10. Calculated spectra resulting from spherical averaging over the angle $\Delta\theta=6^\circ$ of electron incidence. Light detection angles $\alpha=35^\circ$ (a) and $\alpha=70^\circ$ (b). (c) and (d) as (a) and (b) but multiplied with the Fermi function at room temperature and convoluted with Gaussians of FWHM=0.45 (0.35) eV.

tween the majority and minority part of the surface state is more or less interchanged in the theoretical analysis.

To overcome these deficiencies we recalculated the spectra taking into account the finite experimental angular resolution in the electron incidence. In particular, we calculated spherically averaged spectra considering a cone of electron incidence, which corresponds to $\Delta\theta=6^\circ$. The resulting raw spectra are shown in Figs. 10(a) and 10(b) for the two photon takeoff angles. A minority surface structure is visible, which disperses slightly to lower energies with increasing k_{\parallel} . There is also a majority surface state found, lower in energy at $\bar{\Gamma}$, which, however, disperses to higher energies while losing spectral weight. This dispersion behavior is consistent with IPE data for off-normal electron incidence.⁶⁸ According to our calculations, in certain directions of the surface Brillouin zone, the majority state even splits into two states with different dispersion behavior. The expected scenario with one pair of spin states is not valid for Fe with its large spin splitting compared with the bandwidth. Hybridization between s , p , and d states with their different spin splitting results in a band order that is different for the two spin systems and so are the conditions for surface states to form. With the assumption of a small, but finite angular distribution of the incoming electrons, the high-energy wing of the observed majority spectral feature is explained to be caused by the positive dispersion behavior of the surface state. This is clearly visible in Figs. 10(c) and 10(d), in which we show the raw spectra multiplied by the Fermi function and convoluted with a Gaussian of FWHM=0.45 (0.35) eV. Also the puzzle connected with the intensities of the majority and minority surface emissions is solved by taking into account a finite angular resolution in the theoretical analysis. Last but not least, the exchange splitting calculated for normal electron incidence completely vanishes in the spherically averaged spectra. Even the experimental finding of an almost reversed spin splitting looks reasonable.

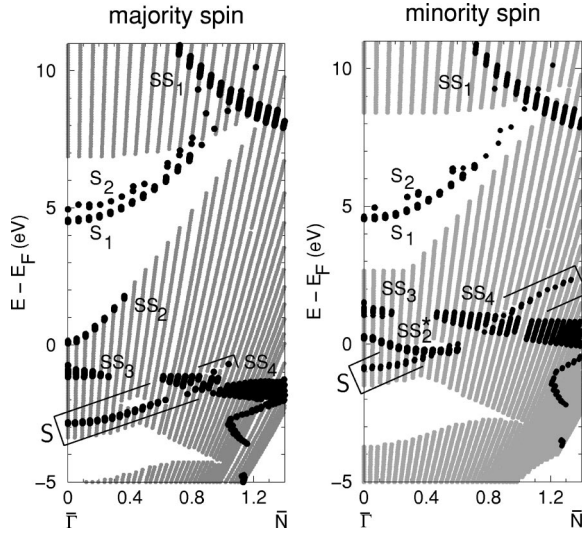


FIG. 11. Projected bulk band structure for majority-(left panel) and minority-spin character (right panel) along $\bar{\Gamma}\bar{N}$ direction. Shaded regions represent bulk states. Filled black circles represent surface features. S_1 and S_2 denote first and second image potential states. S denotes an occupied surface state. The features denoted by SS_1 , SS_2 , SS_3 , and SS_4 have been identified as surface resonances.

Although the agreement between experiment and theory is quantitative in the spectroscopical sense, some questions, which are connected to the physical origin of this surface structure, need to be discussed in more detail. None of the surface-related structures, which we measured above E_F , occur in the electronic structure calculation. On the other hand, they dominate the spectroscopic results. The explanation for this peculiarity can be given in terms of a realistic surface potential, which we only introduced in the spectroscopic analysis. This is because a self-consistent slab calculation, which accurately takes care of a realistic surface barrier, i.e., of a surface barrier with the correct image potential behavior, is by no means a trivial task and not yet generally solved. It is known for a long time that the local-density approximation, and probably gradient-corrected schemes as well, are not able to provide the correct asymptotics of a potential away from the crystal surface. This is not, however, a general shortcoming of the density-functional theory. It has been demonstrated, e.g., by Gunnarsson *et al.*^{69,70} that in the weighted-density approximation, a model function describing the shape of the exchange-correlation hole can be tuned in such a way as to fulfil several physically important limiting conditions, including the $1/z$ asymptotics of the potential outside a solid surface. The *ab initio* calculations incorporating the weighted-density approximation remain, however, relatively rare and have not yet been, to our knowledge, applied to the study of surface-related states. So far, an *ad hoc* adjustment of the potential barrier near the surface remains an arguably workable alternative.

In principle, the situation restricts us in a reliable description of the surface electronic structure. Fortunately, for Fe(110) the problem is solvable since we were able to construct a realistic surface barrier from the spectroscopic data. This z -dependent potential may be used to calculate the dis-

person behavior of crystal-induced and image-potential-induced surface structures. The result is shown in Fig. 11 for the majority-spin channel as well as for the minority-spin channel. The bulk bands of Fe projected along the $\bar{\Gamma}\bar{N}$ direction of the surface Brillouin zone have been visualized by the shaded regions. The dispersion of surface-related features with k_{\parallel} is indicated by solid circles. From these figures the situation becomes more clear. In accordance with our electronic slab calculation and with former investigations²⁴ in both spin channels, a surface feature disperses in the occupied region of the projected bulk band structure. Moreover, a direct comparison between Figs. 7 and 11, i.e., between the slab calculation and the layer-Korringa-Kohn-Rostoker calculation, reveal a quantitative agreement in the dispersion behavior of this spin-split surface state. As a guide to the eye, we marked these features by surrounding them with rectangular frames and labeling them by S in Figs. 7 and 11. The majority peak, which is located in energy at about $E_B^{\uparrow} = 2.8$ eV at $\bar{\Gamma}$ disperses to lower binding energies when approaching the N point. A similar feature, also denoted by S , has been obtained in the minority channel. This peak starts from $\bar{\Gamma}$ at $E_B^{\downarrow} = 1.0$ eV and also disperses upwards in energy.

The first and second image-potential states denoted by S_1 and S_2 can be easily identified by their free-electron-like dispersion. They are totally unoccupied, pinned to the vacuum level, and concentrated with their wave functions in front of the outermost atomic layer. The exchange splitting for the first image-potential state has been calculated to be $\Delta_{ex} = 80$ meV in reasonable agreement with the experimental value of $\Delta_{ex} = 57$ meV.⁶⁵ It should be mentioned here that the parameters for the spin-dependent surface barrier had to be chosen in such a way that they compensate to a certain amount the bulk-induced splitting. Otherwise the calculated spin splitting in the crystal induced as well as in the image-potential-induced surface states would be overestimated by the theory. This surprising result is in perfect agreement with a former analysis of Inglesfield and co-workers on Fe(110).⁷¹ They found that the effect of spin polarization in the surface barrier is rather small and opposite to the bulk contribution. An explanation for this unexpected potential arrangement at the Fe(110) surface had been given in terms of a negative spin density of surface electrons at the Fermi level.

In addition to the image-potential surface states, our calculations exhibit resonancelike structures in both spin channels, which we denoted by $SS_{1,2,3,4}$. For normal electron incidence, i.e., at $\bar{\Gamma}$, it turns out that the most important ones are SS_2 and SS_2^* because these features dominate the spin-resolved inverse-photoemission spectra just above E_F . The spectral weight of SS_3 is very small compared with that of SS_2 and SS_2^* and in fact it is not separable from the bulk d -band emission, neither in photoelectron spectroscopy nor in inverse photoemission. The resonancelike features denoted by SS_1 and SS_4 can also strongly contribute to the total intensity distributions but only for higher angles of electron incidence (emission). This point, of course, has to be confirmed by future experimental investigations. Last but not least, the peculiar dispersion behavior observed for SS_2 and SS_2^* in the calculated spectra becomes quite clear. Due to the

spin-dependent band order in Fe, the spin-dependent surface features SS_2 and SS_2^* have quite different band character and cannot be viewed as spin partners any more. In the majority channel, SS_2 is located highest in energy compared to SS_3 and S and therefore disperses unhindered from E_F at $\bar{\Gamma}$ to higher energies along the gap boundary. As a consequence, a pronounced dispersion to higher energies can be detected. The situation turns out to be completely different in the minority-spin channel. As it has been observed from the theoretical analysis, SS_2^* is located in energy between S and SS_3 in the vicinity of $\bar{\Gamma}$. Between SS_2^* and the gap boundary exists a distance in energy of about 2.5 eV. Also, the small gap observable at $0.4\bar{\Gamma}\bar{N}$ is more or less located in energy at E_F . Taking into account the three points discussed above, it becomes understandable that the surface feature SS_2^* disperses slightly downwards in energy with \mathbf{k}_{\parallel} . To learn more about the symmetry character of SS_2^* we repeated the spectroscopic calculations without considering d states. This procedure keeps SS_2^* alive, but with a switch from negative to positive dispersion such as SS_2 . This means, the negative dispersion behavior is forced by the existence of the d states appearing in the minority channel at these energies.

Kim *et al.*²⁵ recently reported on two surface-sensitive structures, which they observed in a spin-polarized photoemission study on Fe(110) along the $\bar{\Gamma}\bar{S}$ symmetry line. The interpretation was given in terms of an increased charge-density distribution in the first two layers of a 23-layer slab representing Fe(110). These findings definitely support our results because an increased charge density in the surface region may serve as a hint for the existence of surface-sensitive structures such as resonances. Nevertheless, a complete description of surface resonances is closely connected with the presence of a realistic surface barrier,⁷² which was not considered in the slab calculation shown in Ref. 25.

Our theoretical analysis indubitably shows that the surface electronic structure of ferromagnetic Fe(110) not only depends on the bulk- or slab-potential properties. On the contrary, it is dominated by the shape of a realistic surface barrier. One point should be emphasized: for a variety of semi-infinite crystalline materials surface states have been found but only for a few systems such as Cu(100) detailed experimental and theoretical investigations^{61,73} were able to identify resonancelike features. One explanation may be found in the experimentally prepared surface conditions. Only the very clean Fe(110) surface exhibits surface resonances, which were not observed in former IPE investigations on Fe(110).^{26,28} In our experiment, we deposited ultrathin Fe films on W(110), while in earlier experiments the (110) surface of a bulk iron single crystal with its bulk im-

purities had to be cleaned. In other words, one needs a very clean and well-prepared surface to be able to detect a resonancelike structure. In addition one has to keep in mind that the resonance observed on Cu(100) is essentially of sp character, whereas the resonances, which we found on Fe(110) are mainly related to relatively narrow d bands dispersing around the Fermi level. This explains why the intensity distribution of the resonancelike feature on Fe is much more pronounced than on Cu, even dominating the spectral distribution at $\bar{\Gamma}$ against the ordinary bulk d -band emission in iron. Since this behavior is not expected to be an exclusive characteristic of Fe, corresponding analyses for other elements are under way.

V. SUMMARY

In our study on Fe(110), we have observed a complex surface-state behavior at a magnetic surface. In addition to the minority d -band transition and the exchange-split, image-potential state, a third structure was observed on Fe(110) located in energy just above the Fermi level. This peak, identified as a surface resonance, reveals an unexpected spin splitting and a peculiar dispersion behavior. Due to the spin-dependent energetic band order in Fe, the two surface features have quite different band characters and cannot be viewed as spin partners any more. Since slab calculations do not include a realistic surface barrier yet, they could not reproduce the experimentally observed features. One-step model calculations including a realistic surface barrier with parameters given from the experiment are able to model the experimentally observed situation. Since, however, only slab calculations can provide layer-dependent magnetic moments, it is not possible to draw a conclusion about a possible surface-state contribution to the surface magnetic moment of Fe(110) at this stage. Combined experimental investigations below and above the Fermi level are needed to learn more about the impact of surface states on the magnetic behavior of surfaces. Our study shows that layer-dependent, spin-density calculations that include a realistic surface potential are necessary to describe the surface magnetic properties on the basis of the spin-dependent electronic structure.

ACKNOWLEDGMENTS

Financial support from the Deutsche Forschungsgemeinschaft is gratefully acknowledged. This work was supported in part by the BMBF within the Verbundprojekt "Elektronische Struktur und Photoemission von hochkorrelierten intermetallischen seltenen Erdverbindungen" (Contract No. 05605MPA0).

¹*Band-Ferromagnetism: Ground-State and Finite-Temperature Phenomena*, edited by K. Baberschke, M. Donath, and W. Nolting (Springer, New York, 2001).

²V. Dose, *Prog. Surf. Sci.* **13**, 225 (1983); *Surf. Sci. Rep.* **5**, 337 (1985); G. Borstel and G. Thörner, *ibid.* **8**, 1 (1988); N.V. Smith,

Rep. Prog. Phys. **51**, 1227 (1988).

³M. Donath, *Surf. Sci. Rep.* **20**, 251 (1994).

⁴M. Donath, *J. Phys.: Condens. Matter* **11**, 9421 (1999).

⁵M. Donath, F. Passek, and V. Dose, *Phys. Rev. Lett.* **70**, 2802 (1993).

- ⁶M. Donath, B. Gubanka, and F. Passek, *Phys. Rev. Lett.* **77**, 5138 (1996).
- ⁷M. Donath, V. Dose, K. Ertl, and U. Kolac, *Phys. Rev. B* **41**, 5509 (1990).
- ⁸K. Starke, K. Ertl, and V. Dose, *Phys. Rev. B* **45**, 6154 (1992).
- ⁹B. Gubanka, M. Donath, and F. Passek, *Phys. Rev. B* **54**, R11 153 (1996).
- ¹⁰F. Schedin, D.R. Warburton, G. Thornton, and M.A. Hoyland, *Phys. Rev. B* **57**, 3491 (1998).
- ¹¹F.J. Himpsel and D.E. Eastman, *Phys. Rev. Lett.* **41**, 507 (1978).
- ¹²G. Borstel, G. Thörner, M. Donath, V. Dose, and A. Goldmann, *Solid State Commun.* **55**, 469 (1985).
- ¹³J. Kutzner, R. Pauksch, C. Jabs, H. Zacharias, and J. Braun, *Phys. Rev. B* **56**, 16 003 (1997).
- ¹⁴F.J. Himpsel and D.E. Eastman, *Phys. Rev. B* **20**, 3217 (1979); **21**, 3207 (1980).
- ¹⁵C. Math, J. Braun, and M. Donath, *Surf. Sci.* **482-485**, 556 (2001).
- ¹⁶P. Heimann and H. Neddermeyer, *Phys. Rev. B* **18**, 3537 (1978).
- ¹⁷A. Schultz, R. Courths, H. Schultz, and S. Hüfner, *J. Phys. F: Met. Phys.* **9**, L41 (1979).
- ¹⁸A.M. Turner, A.W. Donoho, and J.F. Erskine, *Phys. Rev. B* **29**, 2986 (1983).
- ¹⁹R. Kurzawa, K.P. Kämper, W. Schmitt, and G. Güntherodt, *Solid State Commun.* **60**, 777 (1986).
- ²⁰M. Getzlaff, Doctoral thesis, Universität Bielefeld, 1993.
- ²¹Y. Sakisaka, Th. Rhodin, and D. Mueller, *Solid State Commun.* **53**, 793 (1985).
- ²²E. Vescovo, C. Carbone, and W. Eberhardt, *Phys. Rev. B* **48**, 285 (1993).
- ²³D.G. Dempsey, L. Kleinman, and E. Caruthers, *Phys. Rev. B* **13**, 1489 (1976).
- ²⁴J. Redinger, C.L. Fu, A.J. Freeman, U. Knig, and P. Weinberger, *Phys. Rev. B* **38**, 5203 (1988).
- ²⁵H.J. Kim, E. Vescovo, S. Heinze, and S. Blügel, *Surf. Sci.* **478**, 193 (2001).
- ²⁶A. Santoni and F.J. Himpsel, *Phys. Rev. B* **43**, 1305 (1991).
- ²⁷F.J. Himpsel, *Phys. Rev. B* **43**, 13 394 (1991).
- ²⁸H. Scheidt, M. Glöbl, V. Dose, and J. Kirschner, *Phys. Rev. Lett.* **51**, 1688 (1983).
- ²⁹E. Bertel and M. Donath, *Electronic Surface and Interface States on Metallic Systems* (World Scientific, Singapore, 1995).
- ³⁰U. Gradmann and G. Waller, *Surf. Sci.* **116**, 539 (1982).
- ³¹U. Gradmann, J. Korecki, and G. Waller, *Appl. Phys. A: Solids Surf.* **A39**, 101 (1986).
- ³²H.J. Elmers and U. Gradmann, *Appl. Phys. A: Solids Surf.* **A51**, 255 (1990).
- ³³J. Glazer and E. Tosatti, *Solid State Commun.* **52**, 11 507 (1984).
- ³⁴M. Landolt, *Appl. Phys. A: Solids Surf.* **A41**, 83 (1986).
- ³⁵J. Kirschner and K. Koike, *Surf. Sci.* **273**, 147 (1992).
- ³⁶G. Schönhense and H.C. Siegmann, *Ann. Phys. (N.Y.)* **2**, 465 (1993).
- ³⁷V. Dose, Th. Fauster, and R. Schneider, *Appl. Phys. A: Solids Surf.* **A40**, 203 (1986).
- ³⁸C. Math, R. Fischer, S. Bassen, V. Dose, and M. Donath (unpublished).
- ³⁹U. Kolac, M. Donath, K. Ertl, H. Liebl, and V. Dose, *Rev. Sci. Instrum.* **59**, 1933 (1988).
- ⁴⁰D. J. Singh, *Planewaves, pseudopotentials and the LAPW method* (Kluwer Academic Publishers, Boston, 1994).
- ⁴¹P. Blaha, K. Schwarz, and J. Luitz, WIEN97 (Vienna University of Technology, Vienna, 1997), improved and updated UNIX i version of the original copyrighted WIEN code, which was published by P. Blaha, K. Schwarz, P. Sorantin, and S. B. Trickey, *Comput. Phys. Commun.* **59**, 339 (1990).
- ⁴²J.P. Perdew, K. Burke, and M. Ernzerhof, *Phys. Rev. Lett.* **77**, 3865 (1996).
- ⁴³A.K. Rajagopal and J. Callaway, *Phys. Rev. B* **7**, 1912 (1973).
- ⁴⁴M.V. Ramana and A.K. Rajagopal, *Adv. Chem. Phys.* **54**, 231 (1983).
- ⁴⁵F. Calogero, *Variable Phase Approach to Potential Scattering* (Academic Press, New York, 1967).
- ⁴⁶H. Ebert and B.L. Gyorffy, *J. Phys. F: Met. Phys.* **18**, 451 (1988).
- ⁴⁷A. Gonis, *Green functions for ordered and disordered systems*, *Studies in Mathematical Physics Vol. 4* (North Holland Publisher, Amsterdam, 1992).
- ⁴⁸X. Wang, X.G. Zhang, W.H. Butler, G.M. Stocks, and B.N. Harmon, *Phys. Rev. B* **46**, 9352 (1992).
- ⁴⁹S.C. Lovatt, B.L. Gyorffy, and G.Y. Guo, *J. Phys.: Condens. Matter* **5**, 8005 (1993).
- ⁵⁰W. Kohn and N. Rostoker, *Phys. Rev.* **94**, 1111 (1954).
- ⁵¹A.R. Williams and J. van W. Morgan, *J. Phys. C* **7**, 37 (1974).
- ⁵²R. Feder, *J. Phys. C* **14**, 2049 (1981).
- ⁵³R.G. Brown and M. Ciftan, *Phys. Rev. B* **27**, 4564 (1983).
- ⁵⁴A. Gonis, X.G. Zhang, and D.M. Nicholson, *Phys. Rev. B* **40**, 947 (1989).
- ⁵⁵X.G. Zhang, A. Gonis, and J.M. MacLaren, *Phys. Rev. B* **40**, 3694 (1989).
- ⁵⁶W.H. Butler and R.K. Nesbet, *Phys. Rev. B* **42**, 1518 (1990).
- ⁵⁷R.K. Nesbet, *Phys. Rev. B* **41**, 4948 (1990).
- ⁵⁸W.H. Butler, A. Gonis, and X.G. Zhang, *Phys. Rev. B* **45**, 11 527 (1992).
- ⁵⁹J.B. Pendry, *Surf. Sci.* **57**, 679 (1976); J.F.L. Hopkinson, J.B. Pendry, and D.J. Titterton, *Comput. Phys. Commun.* **5**, 599 (1980).
- ⁶⁰J. Braun, *Rep. Prog. Phys.* **59**, 1267 (1996).
- ⁶¹M. Grass, J. Braun, G. Borstel, R. Schneider, H. Dürr, Th. Fauster, and V. Dose, *J. Phys.: Condens. Matter* **5**, 599 (1993).
- ⁶²O.K. Andersen, *Phys. Rev. B* **12**, 3060 (1975).
- ⁶³O.K. Andersen and O. Jepsen, *Phys. Rev. Lett.* **53**, 2571 (1984).
- ⁶⁴G. Malmström and J. Rundgren, *Comput. Phys. Commun.* **19**, 263 (1980).
- ⁶⁵F. Passek, M. Donath, K. Ertl, and V. Dose, *Phys. Rev. Lett.* **75**, 2746 (1995).
- ⁶⁶A.J. Freeman and C.L. Fu, *J. Appl. Phys.* **61**, 3356 (1987); C.L. Fu and A.J. Freeman, *J. Magn. Magn. Mater.* **69**, L1 (1987).
- ⁶⁷R. Wu and A.J. Freeman, *Phys. Rev. Lett.* **69**, 2867 (1992).
- ⁶⁸F. Passek, Doctoral thesis, Universität Bayreuth, 1994.
- ⁶⁹O. Gunnarsson, M. Jonson, and B.I. Lundqvist, *Phys. Rev. B* **20**, 3136 (1979).
- ⁷⁰R.O. Jones and O. Gunnarsson, *Rev. Mod. Phys.* **61**, 689 (1989).
- ⁷¹M. Nekovee, S. Crampin, and J.E. Inglesfield, *Phys. Rev. Lett.* **70**, 3099 (1993).
- ⁷²G. Borstel and J. E. Inglesfield, in *Electronic States on Metal Surfaces*, edited by K. Horn and M. Scheffler, *Handbook of Surface Science Vol. 2* (Elsevier Science, North-Holland, 2000).
- ⁷³G. Thörner, G. Borstel, V. Dose, and J. Rogozik, *Surf. Sci. Lett.* **157**, L379 (1985).